nature photonics

Supplementary information https://doi.org/10.1038/s41566-025-01665-6

Ultracompact multibound-state-assisted flat-band lasers

In the format provided by the authors and unedited

Table of Contents

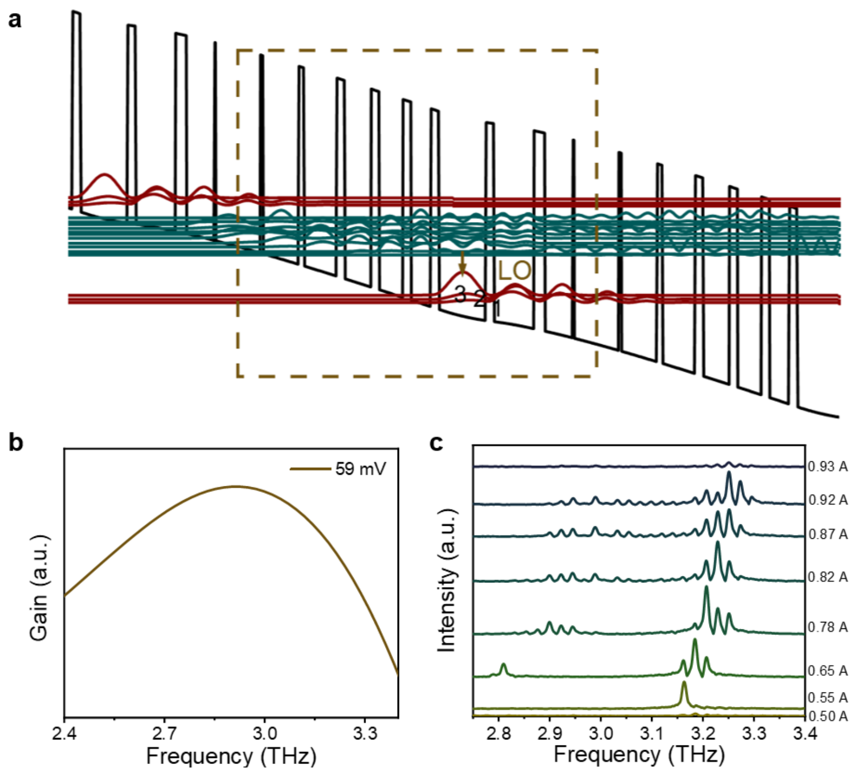

Fig. S1 | The electronic properties of the quantum cascade wafer used in our flat-band lasers. **a,** Conduction band profile and electron wavefunctions with a bias voltage of 59 mV/module. The golden dash box indicates a single period of the active region. **b,** The calculated gain profile of the terahertz (THz) quantum cascade laser (QCL) with a bias voltage of 59 mV/module. **c,** Emission spectra at different pump currents of a conventional ridge laser fabricated on the same quantum cascade wafer. The gain bandwidth is around 2.8-3.4 THz with gradually blue-shifted with increasing pumping, due to the Stark shift of the intersubband transition in the THz QCL medium[1]. The wafer used in this work is the same as used in Ref. [2]. The overall thickness of the wafer is ~18.3 μm. The active region consists of 131 repeat periods. Each period consists of a series of alternating barriers ($Al_{0.15}Ga_{0.85}As$) and quantum wells (GaAs) with the thickness of **1**/12.9/**2**/11.8/**3**/9.5/**3**/8.6/**3**/7.1/**3**/17/**3**/14.5/**4**/10.1/**0.5**/16.2 nm, where bold numbers refer to the $Al_{0.15}Ga_{0.85}As$ barriers. The central 17 nm GaAs well is n-doped with Si at 2.0×10^{16}. The electron wavefunctions as well as the intersubband transition process in each period of the THz QCL are calculated (**a**) by using the tight-binding model. The corresponding gain profile in each period is also calculated (**b**) with the same bias voltage of 59 mV as in **a**.

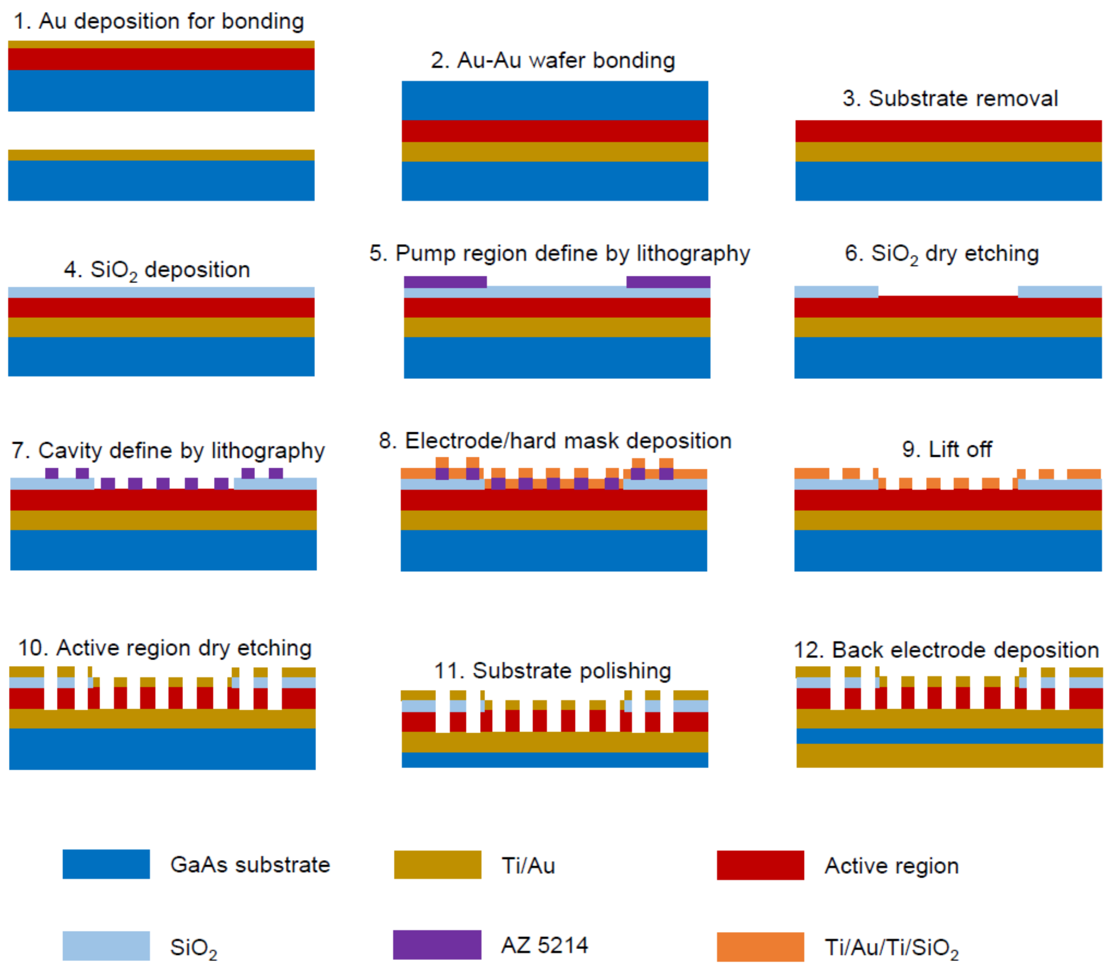

Fig. S2 | Schematic illustration of the fabrication flow for the THz QCL cavities. Ti (15 nm)/Au (700 nm) metal layers were first deposited on the n^+ doped GaAs substrate and the QCL wafer by using an electron-beam evaporator, followed by the Au/Au thermo-compression wafer bonding to form the bottom contact Au layer. After then, the QCL wafer substrate was thinned to be around ~50 μm by a polishing instrument (MULTIPREP™ POLISHING SYSTEM - 8", ALLIED, HIGH TECH PRODUCTS, iNC., USA). The remaining GaAs substrate and $Al_{50}Ga_{50}As$ etch stop layers were then removed by a wet etching process with citric acid/H_2O_2/H_2O (100 g/30 ml/100 ml) and hydrofluoric acid (49%) solution, respectively (we note that the transfer between different solutions have to be fast to reduce the exposure time to air to achieve complete substrate removal for good ohmic contact with the top Au layer). We then deposited 200 nm-SiO_2 insulation layers onto the exposed QCL active medium. To define the pumping region and avoid unexpected whisper-gallery modes caused by gain spreading outside the cavity, photolithography and reactive-ion etching (RIE) were performed to remove the SiO_2 layer in the cavity center while two periods at the edge were preserved. The photonic crystal structure was defined on the QCL wafer by photolithography, followed by deposition and lift-off of contact layers (Ti/Au/Ti/SiO_2, 20/350/20/710 nm) on top of the daisy-like air hole region. Through a reactive-ion dry etching process performed on the active region with a gas mixture of Cl_2/BCl_3/CH_4 = 5/100/20 standard cubic centimeters per minute. We achieved the photonic structures with the contact layers in the remaining area acting as a hard mask. The top Ti/SiO_2 would have ~300 nm residual after dry etching and were removed by RIE process. The exposed Ti/Au layer (350 nm) would act as the top contact metal layer for current injection. The host substrate was thinned to ~200 μm to reduce the impedance for less heat generation, followed by Ti/Au layer (20/250 nm) deposition as bottom electrode. The as-prepared devices were cleaved, indium-soldered onto a copper pedestal, wire-bonded, and fixed onto a cold finger in a cryostat for measurement.

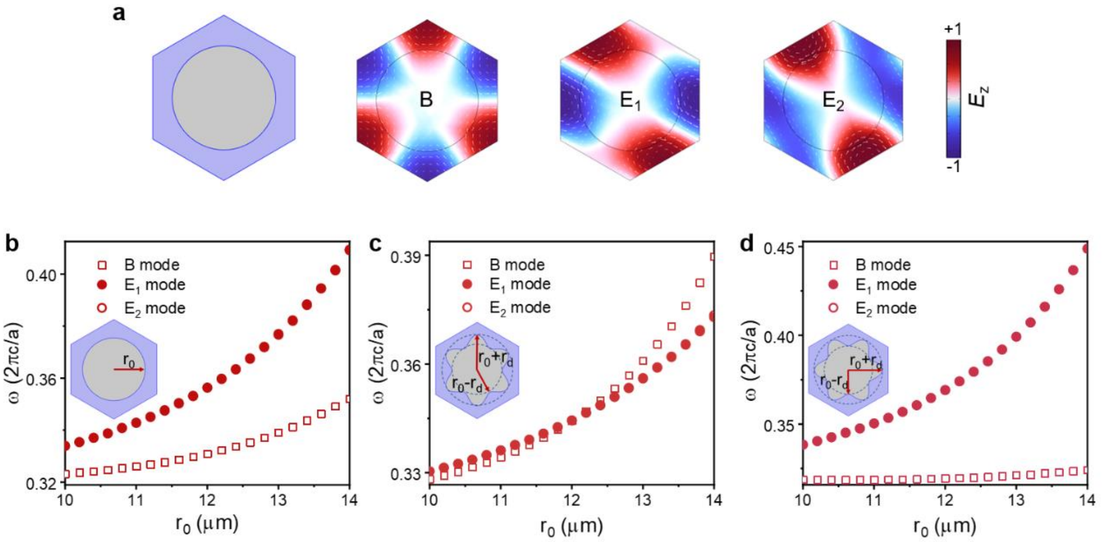

Fig. S3 | Modulation of the photonic band structure. a, Electric field distribution of B, E_1, and E_2 modes in a typical C_6-symmetric lattice. **b-d,** Eigenfrequency of the three modes as a function of r_0 for cavities with circular air hole (**b**), daisy-like air hole (**c**) can be written as $r(\phi) = r_0 - r_d \cos(6\phi)$, and daisy-like air hole with 30˚ rotation (**d**) can be written as $r(\phi) = r_0 + r_d \cos(6\phi)$. Here $a = 33$ μm and $r_d = 2$ μm.

The formation of the Dirac-like band feature requires the degeneracy of B mode, E_1 mode, and E_2 mode, which is realized by manipulating the geometric parameter, as shown in Fig. 2a and Fig. S6a. The k-space engineering starts from a normal C_{6v} structure with circular air hole. The electric field (E_Z) of the three modes are shown in **a**. The eigenfrequency of each mode at the Γ point can be modulated by tuning the radius of air holes (**b**). While the modulation is not strong enough, the frequency of E_1 and E_2 modes are higher than B mode and the degeneracy can only be achieved when the air hole is quite small (corresponding radius not shown in the figure), which will increase the fabrication difficulty in our deep etching process (~18.3 μm), and the band aggregation may cause some mode competition issues.

Thus, we introduce the daisy-like air hole (with the "air bulges" towards the corners) to help to manipulate the photonic band structure (**c**). Because the electric field of the B mode concentrate at the corner of a C_{6v}-symmetry lattice, the effective index, which can be described by $n_{eff} = \sqrt{\frac{\varepsilon \int |E_{qcl}|^2 dV_{qcl} + \int |E_{air}|^2 dV_{air}}{\int |E_{qcl}|^2 dV_{qcl} + \int |E_{air}|^2 dV_{air}}}$ with ε as the dielectric permittivity of QCL, of the B mode would be significant reduced, resulting in increased eigenfrequency. Accordingly, the eigenfrequency of E_1

and E_2 mode would be reduced. Thus, the mode degeneracy can be achieved. As comparison, when the air holes are rotated by 30˚ to make the “air bulges” toward the sides, the situation would be opposite, and the degeneracy cannot be realized (**d**).

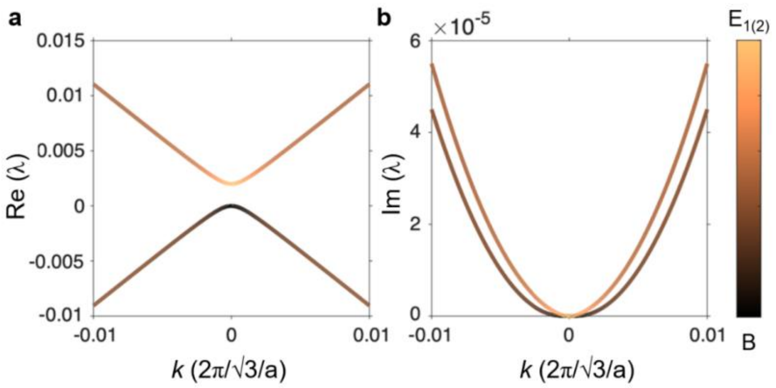

Fig. S4 | Dispersion of the real part (a) and imaginary part (b) of the B and E modes. The brightness of the color indicates the dominance of the E or B mode in the current mode, e.g., brighter colors representing a stronger presence of the E mode. The frequency detuning is $\epsilon = 0.002$ and the group velocity is $\beta = 1$.

We provide a brief discussion of the interaction between singlet B and doublet E modes near the Γ point. Given that the two E modes are coupled with the B mode along the k_x and k_y directions, respectively, we can simplify the interaction between these three modes into a mixing between one of the E modes and the B mode[3],

$$\begin{bmatrix} jk^4 & \beta k \\ \beta k & \epsilon + jk^2 \end{bmatrix} [V_B \quad V_E] = [V_B \quad V_E] \begin{bmatrix} \lambda_B & 0 \\ 0 & \lambda_E \end{bmatrix}$$

where j is the imaginary number, β is the group velocity, ϵ is the frequency detuning, $\lambda_{B(E)}$ and $V_{B(E)}$ are the eigenvalues and eigenvectors of B and E modes at any given Bloch vector k. By taking the eigenvectors at Γ point, $V_{B,0}$ and $V_{E,0}$, as the orthogonal bases, the eigenvectors of B and E modes at vector k can be expressed as,

$$V_B = +aV_{B,0} + bV_{E,0}$$

$$V_E = -bV_{B,0} + aV_{E,0}$$

where coefficients a and b satisfy $a^2 + b^2 = 1$ and can be obtained through orthogonality.

Figure. S4 illustrates the dispersion of both the real and imaginary parts of the eigenvalues, with the color of the lines denoting the mixing of the modes. In **a**, the changing colors on the two bands clearly indicate the mixing between E and B bands as the Bloch vector k drifts away from Γ point. In **b** the loss of B band is smaller than the E band, albeit they both increase as vector k drifts away.

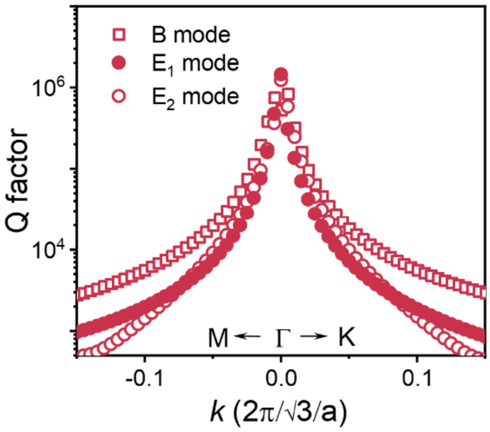

Fig. S5 | Calculated Q factors of B, E_1, and E_2 band in a normal flat-band photonic crystal structure without the introduction of multi-BIC. All the three bands display typical symmetry-protected BIC features with quality factors diverge at the Γ point.

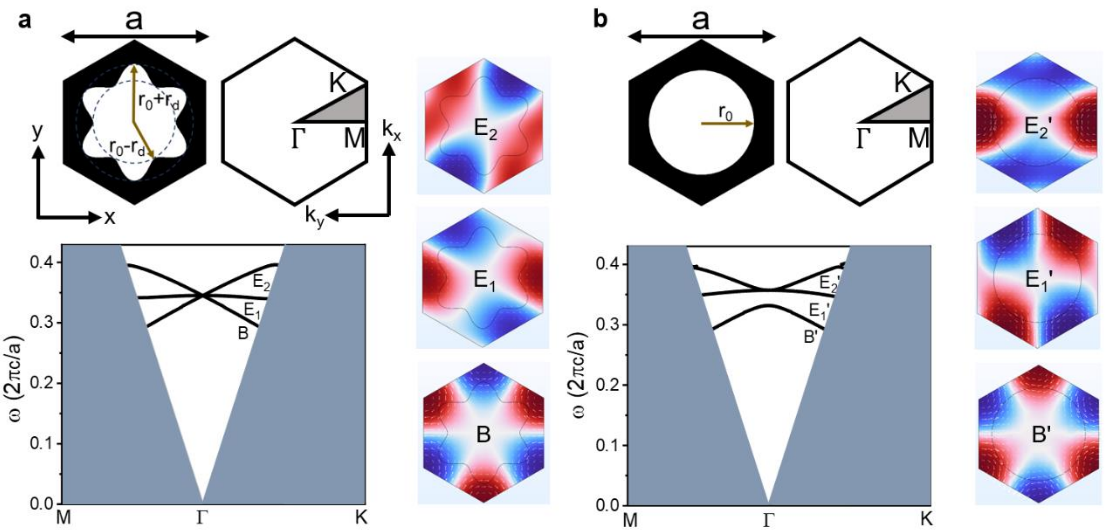

Fig. S6 | Full band structure of the BIC cavities. a, Top, The unit cell and Brillouin zone of the flat-band BIC structure. Bottom, band structure of the flat-band BIC structure. Each band in the figure is named as B, E_1, and E_2, respectively. The bule shades represent the regions below the light cone. Here a metal–semiconductor–metal heterostructure with central dielectric thickness of 18.3 μm is adopted in the simulations. **b,** The unit cell, Brillouin zone, and the full band structure of the "normal C_{6v}-BIC" structure.

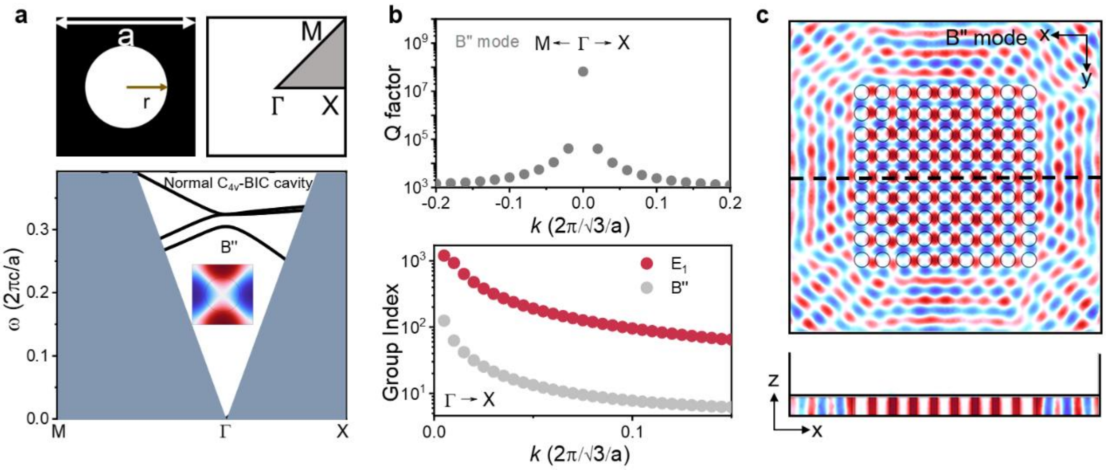

Fig. S7 | BIC mode in a Normal C_{4v}-symmetric cavity. a, The unit cell, Brillouin zone, and the full band structure of the "normal C_{4v}-BIC" cavity. The BIC mode is denoted as B'' mode. Inset, the electric field E_z of B'' mode within a unit cell at the Γ point. **b,** Top, Q factor of the B'' band. Bottom, the comparison of the group index between the designed flat-band BIC mode (E_1 mode) and the normal C_{4v}-BIC mode (B'' mode). The group index of the B'' band with quadratic band dispersion is significantly lower than the E_1 band. **c,** Near-field profiles in finite-size cavities corresponding to the fundamental mode of B'' band. The mode presents a non-localized feature (in-plane) with the electric field substantially leak out of the cavity, because of its weak in-plane feedback.

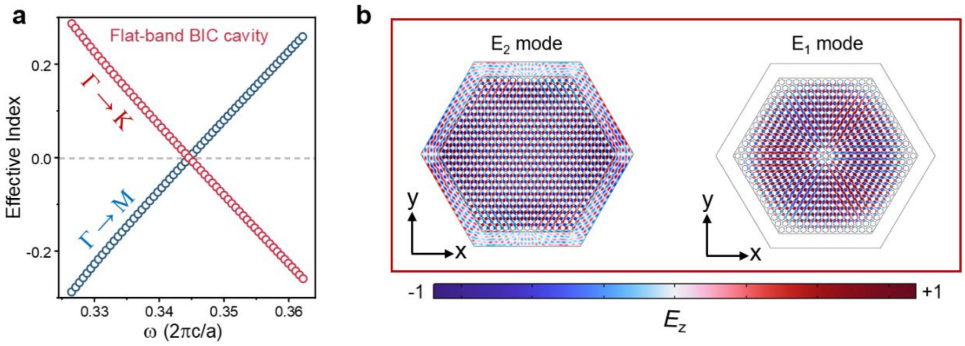

Fig. S8 | Comparison of electric field distribution between the bands with different dispersion behavior. a, Effective index of the two bands with linear dispersion (B and E_2 bands). The effective indices approximate to zero around the Dirac point. **b,** Electric field distribution of another degenerated E_2 mode (left) and the flat-band BIC mode (E_1 mode). As expected, E_1 mode is well confined in the cavity, while E_2 mode with linear dispersion shows a flat field distribution, and lots of field components are leaked out. The huge side leakage losses induced by the linear dispersion (large in-plane group velocity) effectively increase the imaginary free spectral range (iFSR) between the flat-band mode and other adjacent BIC modes, which facilitates the realization of a single-mode operation laser.

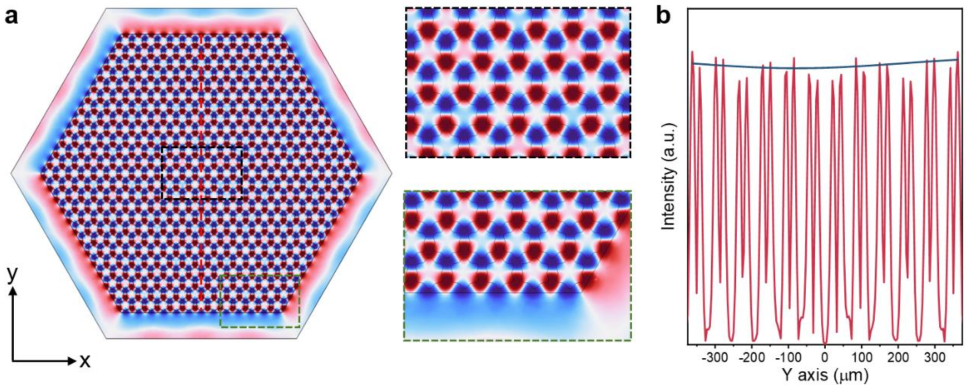

Fig. S9 | Simulated electric field distribution of the B mode with air boundary condition. a, Mode distribution of the B band. As well demonstrated in Ref. 3, the B mode can be well selected when the air boundary is introduced. We note that the huge in-plane side leakage losses still exist in our double-metal QCL case, where only TM mode can be supported in the cavity. **b,** The magnitude of the electric field along the dash cut line (red) as shown in **a**. The uniform field profile across the entire cavity displays an unambiguous effective zero-index material feature, a typical characteristic of a Dirac-cone band structure.

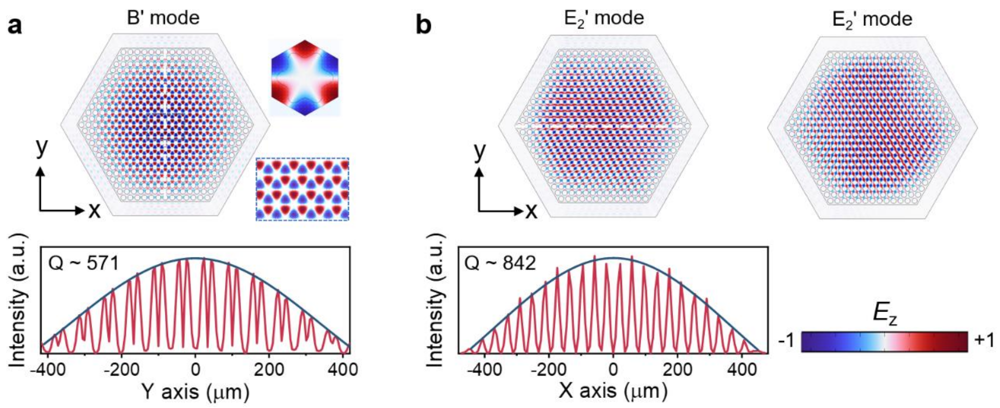

Fig. S10 | Fundamental mode profiles of B' and E_2' bands. a,b, The electric field distribution (top) and extracted magnitude (bottom) of B' (**a**) and E_2' (**b**) bands with quadratic dispersion in normal C_{6v}-BIC cavity (Fig. 2a and Fig. S6b). The magnitude displays a gaussian shape and the fields are tightly confined inside the cavity.

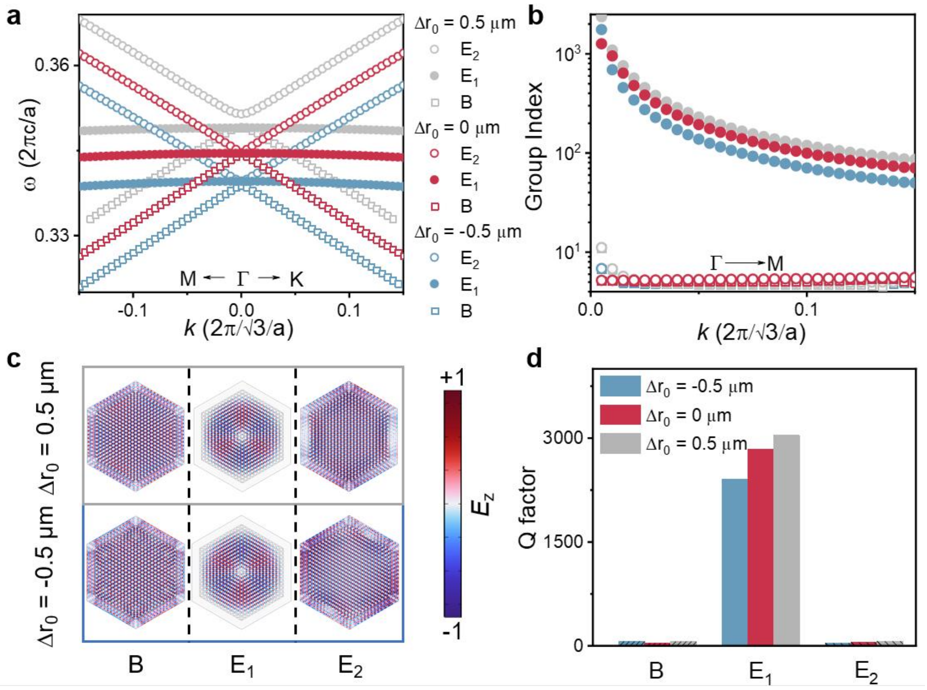

Fig. S11 | Robustness of the Dirac-like band. a, Band structure of the Dirac-like band after taking an $|\Delta r_0|$ = 0.5 μm air hole radius perturbation into consideration. Here Δr_0 represents the radius deviation from the initial design (12 μm) during the fabrication process. **b-d,** Group index (**b**), electric field distribution (**c**), and Q factors (**d**) of each band in (**a**). The results in (**b**) and (**c**) are consistent with each other, which is, a higher group index induces a better in-plane mode confinement, and thus higher Q factor.

We calculated the photonic band structure after taking an air hole radius perturbation of $|\Delta r_0|$ = 0.5 μm into consideration (**a**). The results show that despite the triple intercept point at the Γ = 0 is not a strictly stable point in the parameter space, the effect afforded by the Dirac-like design possess acceptable robustness. The high group index of the E_1 modes and low group index of the B and E_2 modes are barely changed (**b**). We also note that the destroy of the linear dispersion feature of B and E_2 modes would cause a slightly group index enhancement at the vicinity of the Γ = 0. While the enhancement only occurs near the Γ point, the flat-envelope mode profile with large side-leakages in a finite-size cavity will not be impacted (**c**). Thus, the excellent Q contrast between the flat-band mode (E_1) and the other two bands with near-linear dispersion (B and E_2 modes) can be maintained (**d**).

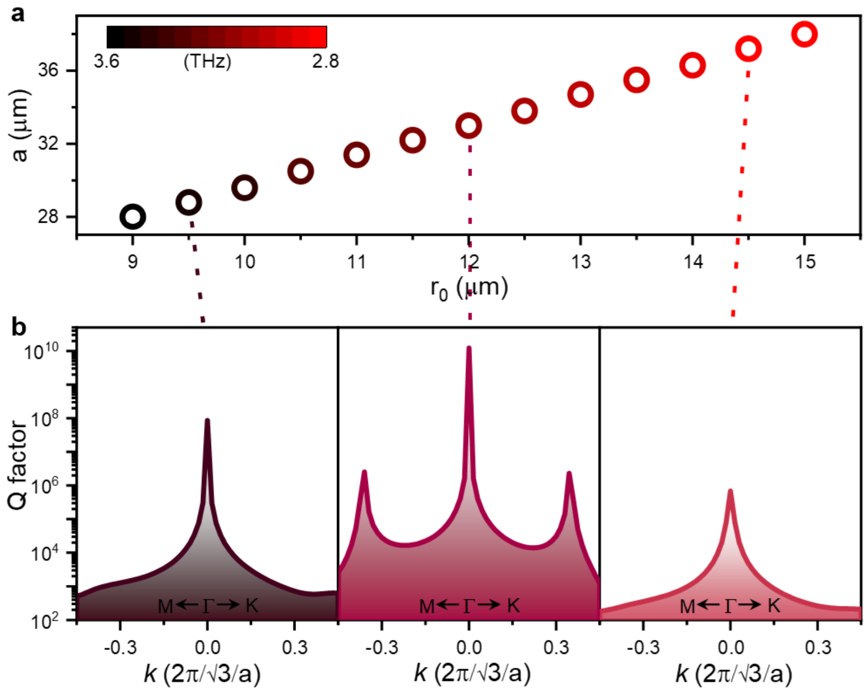

Fig. S12 | Construction of the multi-BIC states. a, Detuning of the lattice parameters to ensure a Dirac-like band feature. The color bar represents the frequency of the three degenerated B, E_1, and E_2 bands at the Γ point. **b,** Calculated Q factors for the lattice with parameters of a = 28.8 μm, r_0 = 9.5 μm (left), a = 33 μm, r_0 = 12 μm (middle), and a = 37.2 μm, r_0 = 14.5 μm (right), here we also set r_d = 2 μm.

The multi-BICs are constructed by fine tuning the lattice constant a. To ensure a Dirac-like band feature, the radius r_0 needs to be adjusted accordingly (**a**). We calculated the Q factors in k space for the lattices with different parameters (**b**). The results illustrate the emergence and disappearance of the accidental-BICs at off-Γ point with the adjustment of lattice structure, accompany with a significant Q factor enhancement in the situation with multi-BIC states (middle). Considering the high-Q factor and the gain range of our QCL wafer, the final parameter with a = 33 μm, r_0 = 12 μm and r_d = 2 μm are applied in the main text.

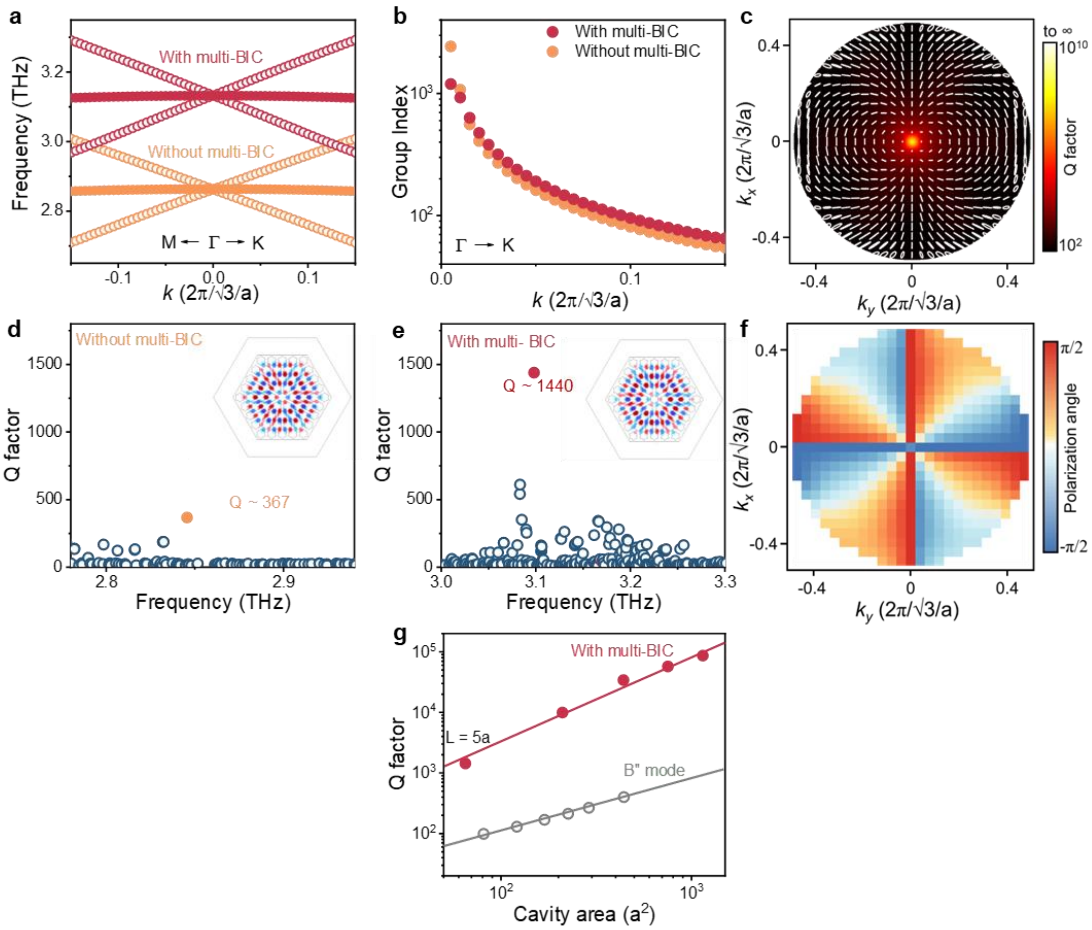

Fig. S13 | Comparison between the flat-band mode with and without multi-BIC. a, Calculated band diagram of a flat-band cavity with (a = 33 μm, r_0 = 12 μm) and without multi-BIC (a = 37.2 μm, r_0 = 14.5 μm). Here, and r_d = 2 μm. **b,** Calculated group index of the flat-band in **a** with and without multi-BIC. **c,** 2D mapping of the Q factor for the flat-band without multi-BIC, the map is darker at off-Γ point than the flat-band with multi-BIC states (Fig. 3a), which means a significant lower Q factor in a finite-size cavity. **d,** Calculated Q factors and mode profile of the flat-band in a cavity without multi-BIC. **e,** Calculated Q factors and mode profile of the flat-band in a cavity with multi-BIC. **f,** Polarization states of the flat-band mode in k space, from which a topological charge of q = +2 can be obtained. **g,** Q factor comparison between flat-band multi-BIC and normal C_{4v}-BIC modes (Fig. S7) in cavities with different area.

The introduction of multi-BIC barely changes the field profile because of the similar band dispersion behavior, but significantly enhances the Q factor from ~367 to ~1440 in a small cavity with a side length of $L = 5a$.

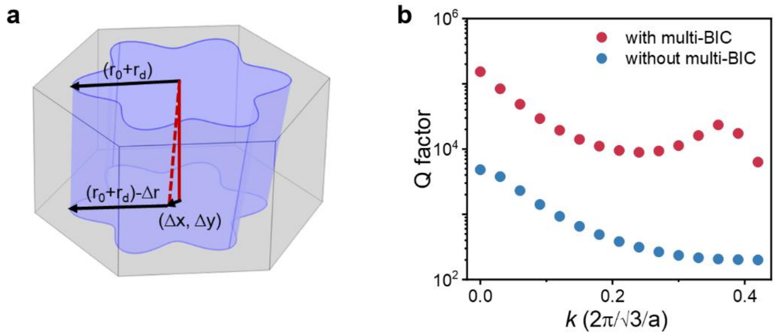

Fig. S14 | Robustness of the multi-BIC modes. a, Schematic of an asymmetric hole acting as a fabrication imperfection, here Δr, Δx, and Δy is set as 0.5 μm based on the actual fabrication accuracy. **b,** Simulated Q factors of the unit cell with disorder. The Q factor of the flat-band mode with multi-BIC states is found to be robust across a range of k values.

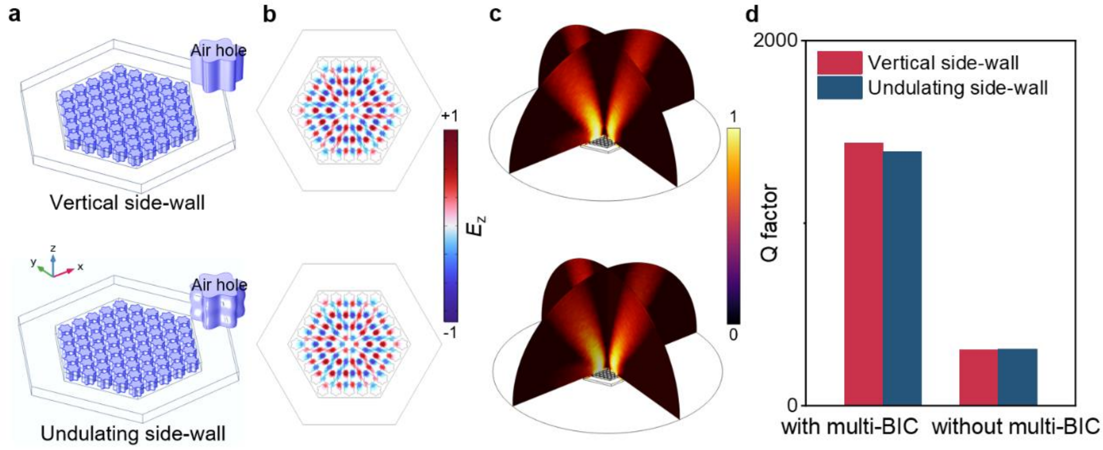

Fig. S15 | Simulation of the flat-band mode with undulating sidewall in L = 5a cavities. a, Schematic of the vertical sidewall (top) and undulating sidewall (bottom) profiles used in the simulation. **b,c,** Electric field distribution **(b)** and beam profile **(c)** for the flat-band BIC mode with vertical sidewall (top) and undulating sidewall (bottom). **d,** Calculated Q values for the flat-band mode with two kinds of sidewalls.

The QCL wafer utilized in this work has a quite thick active region of ~18.3 μm. Thus, the deep etching process is divided into several steps to facilitate us to check the etching progress, which might introduce undulating sidewall profile in the vertical dimension in some cases. To figure out the impact of the undulating sidewall on the flat-band BIC mode, we conducted the simulation within finite-size cavity (**a**) to figure out the impact of the undulating sidewall on the optical properties in real devices. The envelop of the undulating sidewall was simulated by introducing a two-period sinusoidal function disturbance with amplitude of 0.4 μm. The electric field distribution (**b**), the beam shape (**c**), and the Q factors (**d**) are basically the same.

Thus, we conclude that the undulating sidewall profile has no significant impact on the quality factor and optical properties of the flat-band BIC mode, as the photonic lattice symmetry remains undamaged.

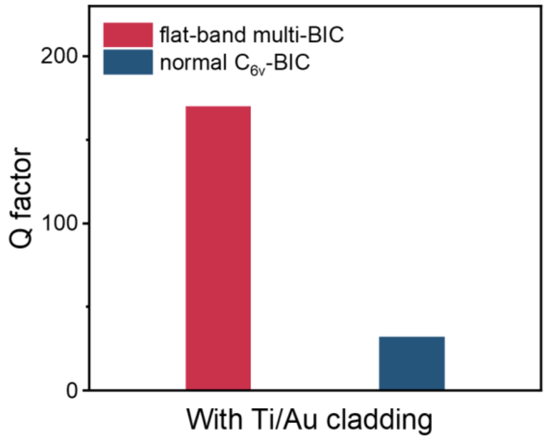

Fig. S16 | Calculated Q factors of the *L* = 5*a* devices incorporating Ti/Au (Drude model) and free carrier absorption, modeled using a complex refractive index of 182.67 + 212.11i[4]. The thickness of the Ti/Au layer is ~350 nm. The Q factor of the flat-band multi-BIC cavity is calculated to be around ~170, which is still significantly higher than the normal BIC cavity (~32) with the same cavity size.

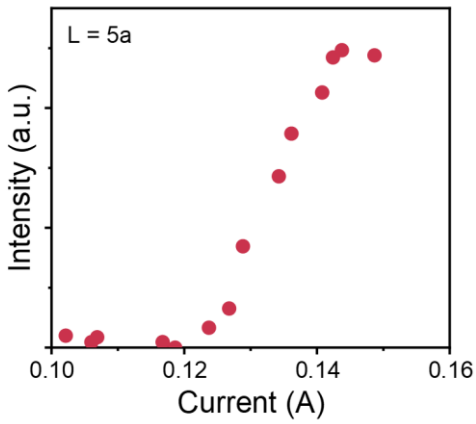

Fig. S17 | Light-current (L-I) curve in an optimized *L* = 5*a* devices. Due to intrinsic current spreading in QCLs[7], the experimentally measured pumping current would be higher than anticipated. To further reduce power consumption, we optimized the device by removing the highly doped layer in the unpatterned region to minimize current spreading, achieving a minimum current of ~125 mA.

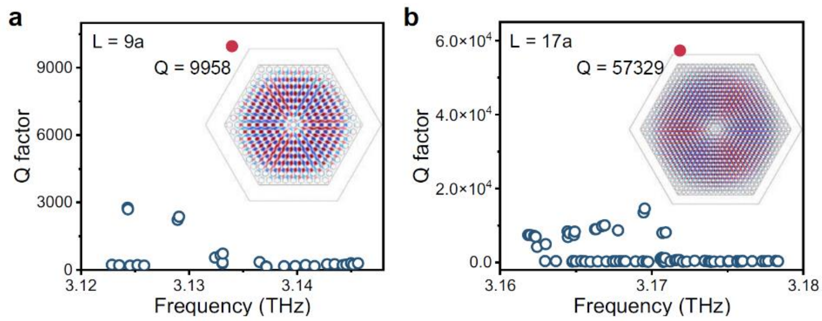

Fig. S18 | Flat-band multi-BIC lasers with different cavity sizes. a, Calculated Q factors and mode profile of a cavity with side length of $L = 9a$. **b,** Calculated Q factors and mode profile of a cavity with side length of $L = 17a$.

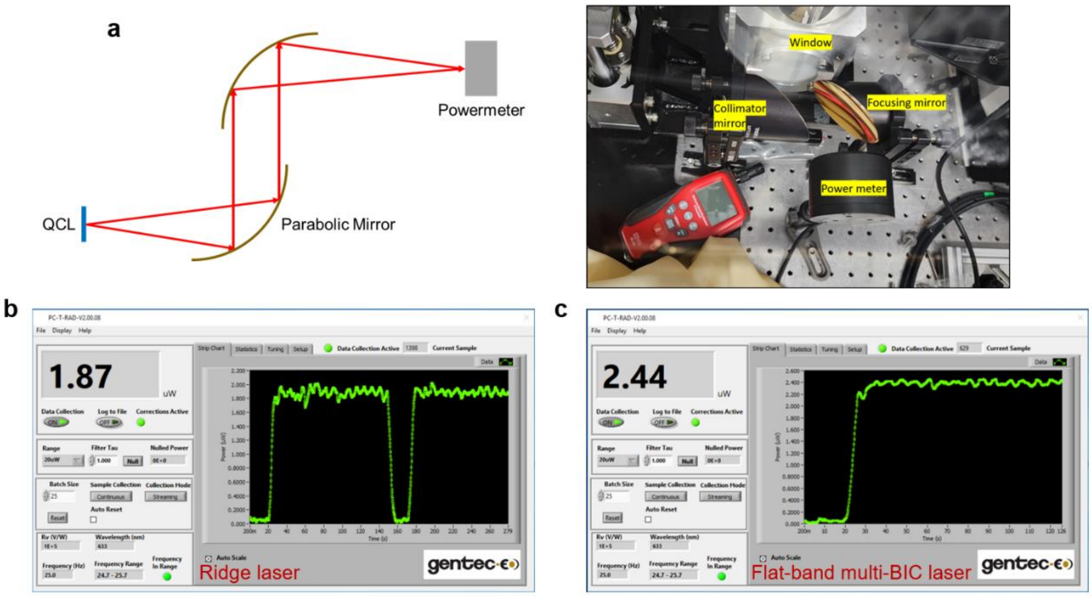

Fig. S19 | QCL power characterisation. a, Setup for focusing the diverged beam of the QCLs. **b,c,** The captured power measurement software screenshot for a typical ridge laser (**b**) with ridge length of 1000 μm and width of 140 μm and the designed flat-band multi-BIC laser (**c**). For comparison, the $L = 9a$ device with similar cavity area (~0.11 mm^2) as the ridge laser (0.14 mm^2) was measured here.

The QCLs power were measured by a terahertz powermeter (Gentec-EO T-Rad with detector head of THZ9B-BL-DZ-D0). The THz detector has a collection aperture of 0.9 mm in diameter. To improve the collection efficiency, the laser emission was focused by two parabolic mirrors, as shown in **a**. The measurement was performed in a dry nitrogen purging circumstance. A correction factor of 2.1 was considered for this powermeter when calculating the peak power.

As a baseline, a typical ridge laser was firstly characterized. The ridge length and width are 1000 μm and 140 μm, respectively. The measured average power is 1.87 μW (**b**), corresponding to a peak power of 0.78 mW. For comparison, the average power of the designed flat-band multi-BIC laser with similar effective pumping area (~0.11 mm^2) was calculated to be 2.44 μW (**c**), corresponding to a peak power of 1.02 mW. The measured flat-band multi-BIC laser even present a higher output power than the ridge laser because of its high collection efficiency brought by the good directivity (see Fig. S20 below).

The results show that the power of the designed laser, which is aimed at good mode confinement and a low current threshold, is indeed not high. While the primary limitation should lie in the quality of the QCL wafer we used.

In addition, we note that for higher output power application, the flat-band cavity without multi-BIC states, which still maintains a Q factor of ~367 (compared to ~60 for traditional band-edge modes with quadratic dispersion, which are unable to lase in such a mall cavity), could be adopted. Because the flat-band feature only enhances the in-plane mode confinement without compromising the power out-coupling efficiency.

We calculated the radiative out-coupling efficiency η_r of the flat-band cavities (Table S2), which is proportional to $Q_{total}/Q_{vertical}$[5], where $Q_{total} = (1/Q_{vertical} + 1/Q_{in\text{-}plane})^{-1}$.

$Q_{vertical}$ can be derived from the equation:

$$Q_{vertical} = \frac{2\pi f}{\gamma_{rad}}$$

where γ_{rad} represent the surface emission loss rate following the equation:

$$\gamma_{rad} = \frac{P_{surf}}{E_{tot}} = \frac{\int_S (\mathbf{E} \times \mathbf{H}) \cdot \mathbf{n}\, dS}{\frac{1}{2}\int_V (\varepsilon \mathbf{E} \cdot \mathbf{E} + \mu \mathbf{H} \cdot \mathbf{H})\, dV}$$

Where P_{surf} represents the power dissipation due to surface emission, and can be estimated by extracting the time-averaged integrated power flow through an air domain upon the resonator, E_{tot} is the total electromagnetic energy stored in the resonator, E and H represent the electric and magnetic fields respectively, ε the permittivity and μ the permeability of the material.

For the flat-band multi-BIC cavity ($L = 5a$), the photon loss rate is calculated to be $\gamma_{rad} = 4.23$ GHz, corresponding to a $Q_{vertical} \approx 4601$. Considering the $Q_{total} \approx 1440$ from the 3D simulation, an out-coupling efficiency of $\eta_r = 31.3\%$ can be obtained. As a comparison, the flat-band without multi-BIC design has a $Q_{total} \approx 367$ and $Q_{vertical} \approx 450$, corresponding to a significantly higher out-coupling efficiency of $\eta_r = 81.6\%$.

Furthermore, when the absorption is considered, the overall Q factor would be $Q_{total} = (1/Q_{vertical} + 1/Q_{in\text{-}plane} + 1/Q_{abs})^{-1}$. We take the absorption loss $\alpha_{abs} = 20$ cm^{-1} (corresponding to a Q value of ~117), the calculated radiative efficiency for the flat-band cavity with and without multi-BIC would be 2.3% and 20.2%, respectively.

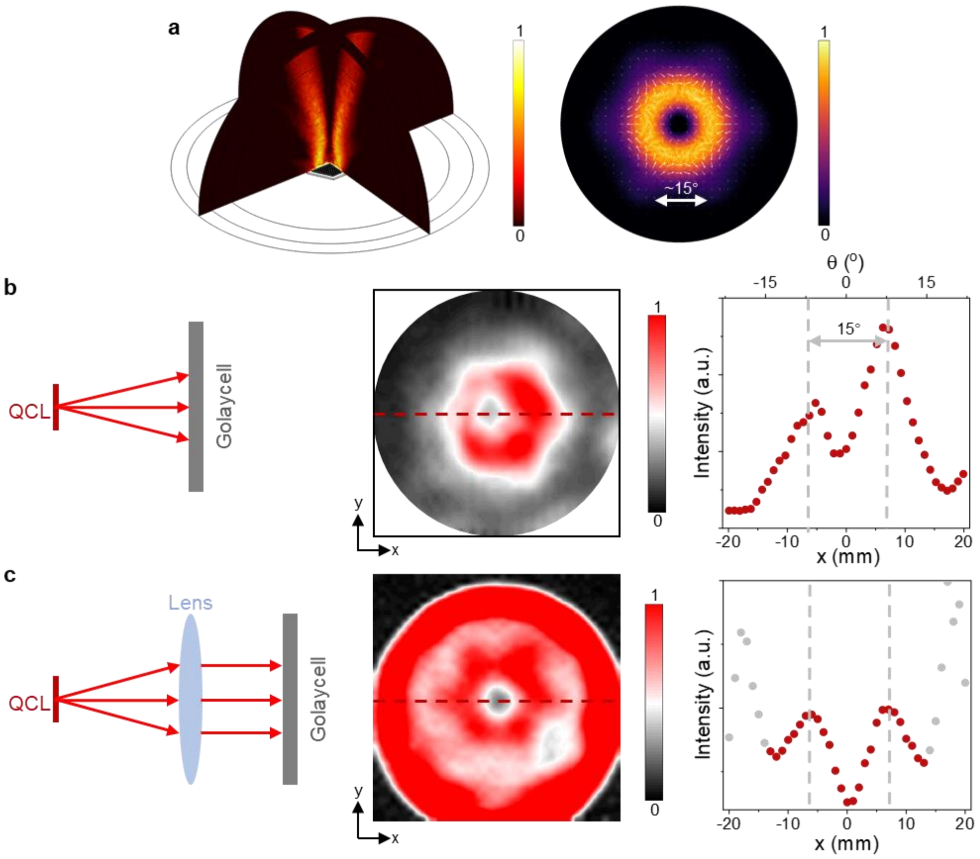

Fig. S20 | Beam pattern characterisation of the designed QCL device (L = 9a). a, Simulated beam profile and far-field pattern. **b,c,** Measured far-field image of the as-prepared flat-band laser without (**b**) and with (**c**) focal lens.

The simulated laser beam of the designed flat-band multi-BIC mode exhibits good directivity with a donut shape far-field pattern (**a**). Such a beam profile with a polarization winding number of $|q| = 2$ can be classified as a type of vector beam.

Experimentally, the far-field image was obtained by collecting the beam intensity with a THz Golay cell detector (TYDEX GC-1T). The Golay cell was mounted on a mechanical arm with a scan step of 1 mm. The detector was approximately 5 cm away from the QCL devices and has an aperture diameter of ~5 mm. The measured far-field image shows a six-fold symmetric beam profile together with an intensity singularity at the centre and a beam divergency approximately ~15˚ (**b**), which matches well with the simulated far-field pattern. The asymmetric intensity distribution might come from the tilt of the test system. We further performed the measurement with a focal lens (**c**), a better result can be obtained. The outer pattern with circular shape should come from the scattering at the edge of the lens.

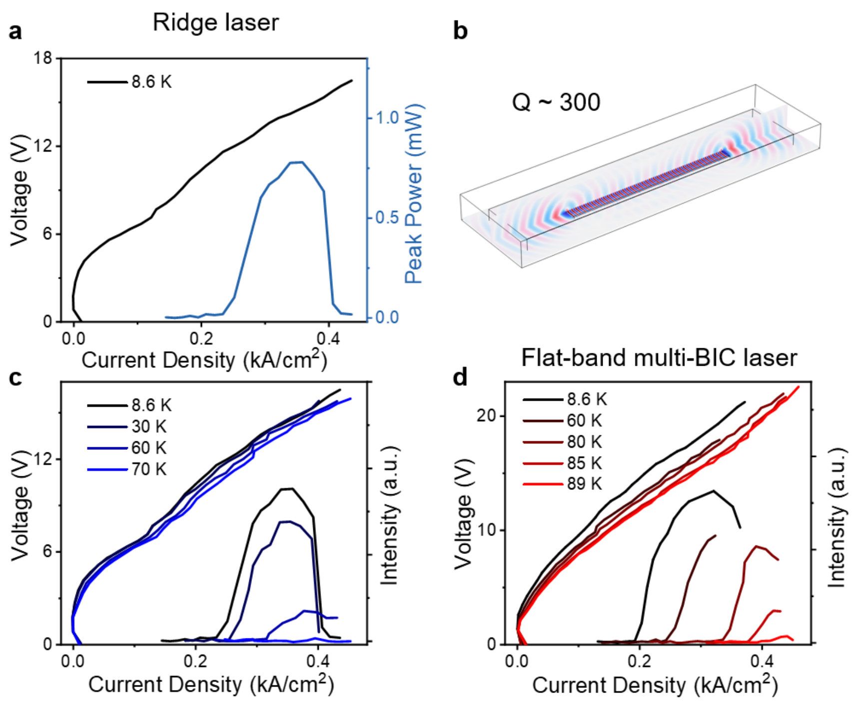

Fig. S21 | Comparison between the designed flat-band multi-BIC laser and a standard double metal ridge laser. a, Light-intensity-voltage curves of the ridge laser. **b,** An simulated F-P cavity mode and its Q factor. **c,d,** L-I-V curves as a function of temperature for the ridge laser (**c**) and the flat-band multi-BIC laser (**d**). (10 kHz repetition rate, 1000 ns pulse width).

We measured a standard double-metal ridge laser with 1000 μm in length, 140 μm in width and 18.3 μm in height. The L-I-V curves are shown in **a**, the ridge laser demonstrates a lasing threshold current density of ~233 A/cm^2, which is ~25% higher than that of the designed flat-band multi-BIC laser (~187 A/cm^2). The maximum lasing temperature of designed flat-band multi-BIC laser (~89 K) is also higher than the double metal ridge laser (~70 K).

In the electrical pumping QCL system with inter-subband transitions, a certain part of voltage is required to establish correct band alignment. Thus, at the beginning, a portion of the injection current is actually due to leakage before the alignment of the structure is reached. After the correct band alignment and population inversion are established, the raised gain (g) will compensate the cavity losses, i.e., α_r and α_{nr}. When the gain is equal to the total losses, $g = \alpha_{tot}$, the lasing action occurs. The current leakage and the absorption α_{nr} are two main intrinsic processes in QCLs. Our flat-band multi-BIC design here focuses on the α_r part, which plays an important role in a compact photonic cavity based on traditional band edge or normal BIC mode (Table S1). The radiative losses α_r in QCL can be written as[6]

$$\alpha = \frac{2\pi * n}{\lambda * Q}$$

Where *n* represents the refractive index, λ is the working wavelength, and Q is the quality factor. The calculated radiative loss of the flat-band multi-BIC mode (Q = 1440) is ~1.6 cm^{-1}, which is much lower than the F-P waveguide mode of ~7.7 cm^{-1} and traditional band edge mode with normal C_{6v}-BIC state (~62.3 cm^{-1}, corresponding to the Q factor of ~37, Fig. 3**b**).

Benefit from the excellent mode confinement in the flat-band multi-BIC cavity by suppressing the out-of-plane (radiative and scattering) losses and in-plane side leakages, as illustrate in the main text, the reduced lasing threshold is finally achieved.

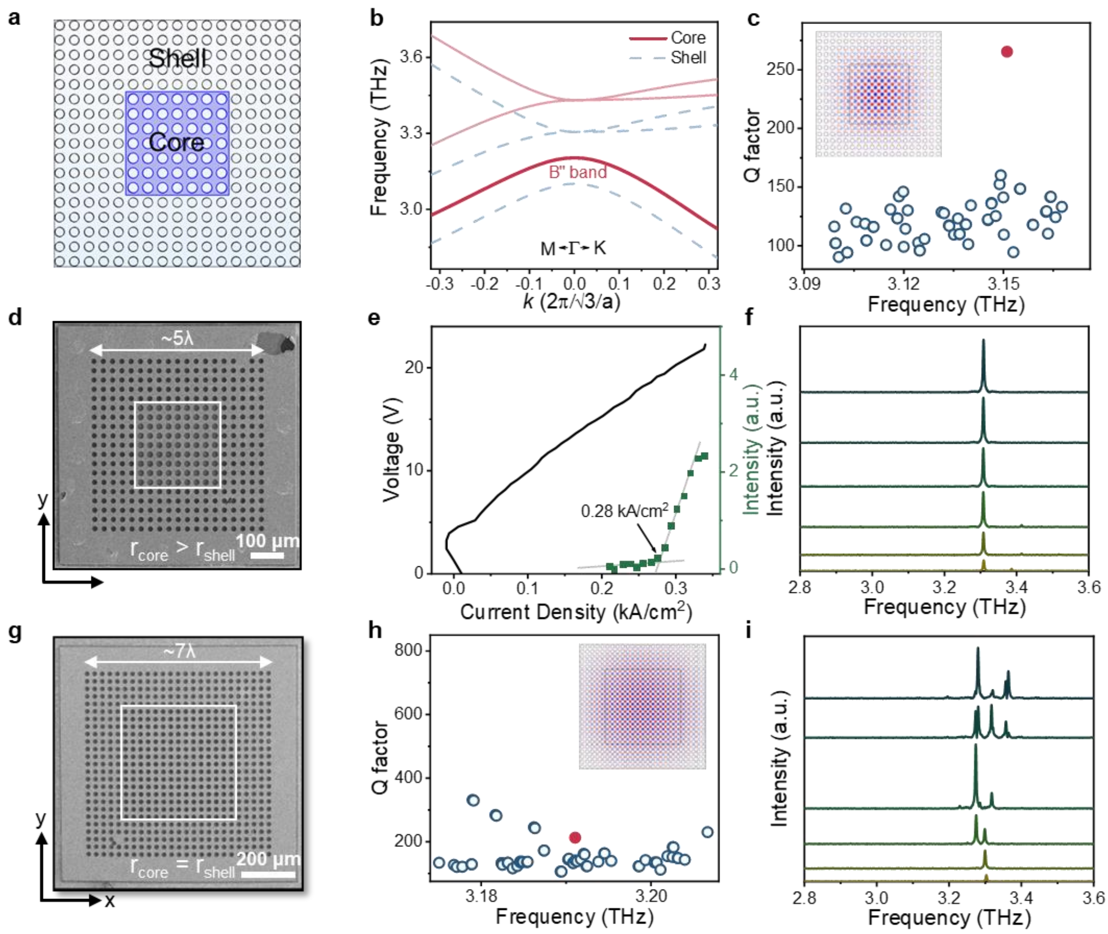

Fig. S22 | BIC lasers with C_{4v} lattice symmetry. a, Schematic of the optimized photonic bandgap (shell)-confined BIC mode (core) as demonstrated in Ref. [8]. **b,** Photonic band diagram of the C_{4v}-symmetry photonic crystals with a = 28 μm and r_{core} (r_{shell}) = 10 μm (9 μm). **c,** Calculated Q factors and mode profile of the photonic bandgap-confined BIC cavity. The Q factor is much lower (~265) than our flat-band multi-BIC mode (~1440) despite the cavity is larger. **d,** SEM image of the fabricated core-shell hetero-structure with r_{core} (10 μm) > r_{shell} (9 μm). Only the core region (inside the white box) is selectively pumped. The overall cavity size is ~5λ. **e,** L-I-V curves of the core-shell cavity with a lasing threshold of ~0.28 kA/ cm^2. **f,** Lasing spectra of the core-shell device, single-mode lasing can be obtained because of the higher Q factor of the BIC mode than the surrounding bulk modes as illustrated in **c**. **g,** SEM image of the traditional “normal C_{4v}-BIC” cavity without optimized core-shell structure, where r_{core} = r_{shell} (10 μm). **h,** Calculated Q factors and mode profile of the traditional BIC cavity. **i,** Lasing spectra of the device based on traditional BIC design. Multi-mode lasing can be observed because the BIC mode is submerged in the bulk modes as shown in **h**.

Type	Frequency (THz)	Cavity Size (λ)	Q-factor	Single-mode	Threshold[&] (kA/cm^2)	Ref.
Flat-band	~3.2	~3	~1440	Yes	~0.19	This work
Multi-BIC	~3.3	~5.4	~9958	Yes	~0.19	
Merging-BIC	~2.9	~5[#]	~342	Yes	~0.8	9
Band-inverted BIC	~2.9	~6[#]	~324	Yes	~2.2	7
Majorana zero mode	~3.4	~8.1	~1000	Yes	~1.2	4
Random laser	~3.3	~5.5[#]	~500	No	~1.5	10
Quasi-crystal laser	~3.3	~8.9[#]	~147	No	~0.6	5
Normal BIC lasers	~2.7	~6.7[#]	~64	Yes	~1.0	11
	~2.9	~4.4[#]	---	Yes	~1.0	12

Table S1 | Comparison of the laser performance between our flat-band multi-BIC and other advanced cavity designs with similar device configuration and fabrication processes.

[#] This value is estimated based on the overall cavity size and lasing wavelength shown in the reference.

[&] The threshold is affected by multiple factors such as the wafer used, fabrication process, and Q factor. It cannot simply be considered to be the result of cavity design. The main purpose of this table is to highlight the compactness and the high-Q of our flat-band multi-BIC design.

Type	Radiative efficiency η_r	Ref.
Flat-band multi-BIC	~31%	This work (L = 5a)
Flat-band without multi-BIC	~83%	
Topological Dirac-vortex	~68%	[6]
Photonic quasi-crystal	~16%	[5]
Topological bulk BIC	~50%*	[7]

Table S2 | Comparison of the radiative efficiency of our flat-band cavity design and other novel photonic crystal-based cavities. All the results in this table only represent the intrinsic radiative efficiency of the designed photonic cavities without considering the waveguide losses.

* This value is estimated based on the Q factors from the references.

References

1 Fathololoumi, S. *et al.* Terahertz quantum cascade lasers operating up to~ 200 K with optimized oscillator strength and improved injection tunneling. *Opt. express* **20**, 3866-3876 (2012).

2 Li, L. *et al.* Broadband heterogeneous terahertz frequency quantum cascade laser. *Electron. Lett.* **54**, 1229-1231 (2018).

3 Contractor, R. *et al.* Scalable single-mode surface emitting laser via open-Dirac singularities. *Nature* **608**, 692-698 (2022).

4 Han, S. *et al.* Photonic Majorana quantum cascade laser with polarization-winding emission. *Nat. Commun.* **14**, 707 (2023).

5 Vitiello, M. S. *et al.* Photonic quasi-crystal terahertz lasers. *Nat. Commun.* **5**, 588 (2014).

6 Liu, J. *et al.* High-power electrically pumped terahertz topological laser based on a surface metallic Dirac-vortex cavity. *Nat. Commun.* **15**, 4431 (2024).

7 Han, S. *et al.* Electrically-pumped compact topological bulk lasers driven by band-inverted bound states in the continuum. *Light Sci. Appl.* **12**, 145 (2023).

8 Ren, Y. *et al.* Low-threshold nanolasers based on miniaturized bound states in the continuum. *Sci. Adv.* **8**, eade8817 (2022).

9 Cui, J. *et al.* Single-mode electrically pumped terahertz laser in an ultracompact cavity via merging bound states in the continuum. *Laser Photon. Rev.* **17**, 2300350 (2023).

10 Zeng, Y. *et al.* Two-dimensional multimode terahertz random lasing with metal pillars. *ACS Photonics* **5**, 2928-2935 (2018).

11 Chassagneux, Y. *et al.* Predictable surface emission patterns in terahertz photonic-crystal quantum cascade lasers. *Opt. express* **17**, 9491-9502 (2009).

12 Chassagneux, Y. *et al.* Graded photonic crystal terahertz quantum cascade lasers. *Appl. Phys. Lett.* **96**, 031104 (2010).